In-situ Non-destructive Phase Boundary Resolving in Metallic Materials

Jiachen Zhang[1,2†], Takamasa Hirai[3†], Pukun Tan[1,2], Ryo Iguchi[3], Fuhua Zhang[4], Xianzhe Chen[5], Cheng Song[6], Zhiyang Wei[7], Dazhi Hou[1,2*], Ken-ichi Uchida[3,8]

[1]International Center for Quantum Design of Functional Materials, Hefei National Research Center for Physical Sciences at the Microscale, University of Science and Technology of China, Hefei, Anhui, 230026, China.

[2]Department of Physics, University of Science and Technology of China, Hefei, Anhui, 230026, China.

[3]National Institute for Materials Science, Tsukuba, 305-0047, Japan.

[4]Hefei Clinical College of Stomatology, Anhui Medical University, Hefei, Anhui, 230001, China.

[5]Frontier Institute of Chip and System, Fudan University, Shanghai, 200000, China.

[6]Key Laboratory of Advanced Materials (MOE), School of Materials Science and Engineering, Tsinghua University, Beijing, 100084, China.

[7]Dongguan Key Laboratory of Interdisciplinary Science for Advanced Materials and Large-Scale Scientific Facilities, School of Physical Sciences, Great Bay University, Great Bay Institute for Advanced Study, Dongguan, 523000, China.

[8]Department of Advanced Materials Science, Graduate School of Frontier Sciences, The University of Tokyo, Kashiwa, 277-8561, Japan.

*Corresponding author(s). E-mail(s): dazhi@ustc.edu.cn;

†These authors contributed equally to this work.

Abstract

Phase boundary, the interface between neighboring physical phases in matter, hosts various emergent novel phenomena and has been a pivotal subject of research interest for decades. Conventional techniques for the spatial resolving of phase boundaries rely on the interaction between the sample and certain probing particles, in which a pristine surface after stringent sample preparation and high vacuum are usually mandatory. Here we show that phase boundaries in metallic alloys can be resolved by the lock-in thermography (LIT) in an ambient environment even in the presence of a coating layer. An alternating charge current is applied through the sample and the phase boundaries are revealed by the Peltier effect therein. We employ the LIT to visualize the propagation of phase boundaries in superelastic NiTi wires during the martensitic phase transition, and demonstrate its capability to detect the martensite phase in a dental rotary file during mechanical bending. Furthermore, imaging of the phase boundaries in FeRh is successfully achieved using the same method, thereby demonstrating its broad applicability. This work offers a general technique for phase boundary visualization in metallic materials, enabling versatile *in-situ* non-destructive defectoscopy of phase-transition alloys in service.

1 Introduction

Phase transitions, which refer to the changes in the crystal structure of materials induced by external factors, play an essential role in optimizing their functionality[1, 2]. These transitions can significantly alter the geometrical, mechanical, thermal, and electrical properties of metals, rendering them vital for a broad range of applications in fields including engineering, medicine, energy storage, and data storage[3–6]. Phase transitions occur in the form of nucleation and growth of the product phase, e.g. martensite phase in martensitic transitions, which forms a moving phase boundary between the parent phase and the product phase, leading to anisotropic strains with a spatially heterogeneous nature. Thus, achieving a thorough understanding of phase transition materials requires spatial resolving of phase distribution, and various technologies such as transmission electron microscopy, scanning electron microscopy, and optical imaging, which often utilize photon or electron beams as probes, have been developed to resolve phase boundaries as illustrated in Fig. 1a[7, 8].

In order to achieve optimal image quality, most conventional characterization techniques rely on stringent sample preparation to ensure a flat and clean sample surface; however, this requirement can hinder accurate phase-resolved measurements in materials that inherently possess rough or uneven surfaces. Moreover, the testing conditions-often involving high vacuum-significantly diverge from service environments, making it difficult to capture authentic *in-situ* behavior. In practical applications, metallic materials frequently serve as complex workpieces with irregular geometries and are commonly covered by opaque oxidation or protective coatings, posing significant obstacles to non-destructive phase boundary imaging under operational conditions[9, 10]. Consequently, data acquired through heavily controlled laboratory settings may not reflect a material's performance in its intended service scenario[11]. Thermal radiation inspection provides a surface-insensitive probing approach. In previous works, the observations of metallic phase transitions were mainly based on the temperature changes arising from the latent heat absorbed or released during the transition, which is inherently transient[12–14]. However, phase boundaries could hardly be resolved by this passive thermographic method, since the latent-heat-induced thermal signal is spatially distributed across the entire transition region and confined to a short observable time window. So the *in-situ* phase boundary imaging of metallic materials in service remains a major challenge in the field of materials science and engineering.

In this work, we introduce an innovative method to visualize phase boundaries in metallic alloys by leveraging the Peltier effect. The Peltier effect generally arises at interfaces between materials with distinct thermoelectric coefficients, e.g. the interfaces between semiconductors of opposite carrier types or two different phases in a host material[15–19]. The Peltier effect has also been utilized successfully to image boundaries between insulating and

metallic phases by thermoreflectance, notably in VO_2[20]. However, due to the inherently weak thermoelectric coefficients of metallic alloys, the associated Peltier signals are significantly smaller[21, 22], thus limiting their broader application in phase boundary imaging. Recently, the lock-in thermography (LIT) has demonstrated sensitivity sufficient to detect temperature variations as minute as 0.1 mK[23], making it capable of resolving subtle Peltier effects, such as the anisotropic magneto-Peltier effect in nickel[24]. Exploiting this high sensitivity, we successfully image phase boundaries in NiTi alloys via the Peltier effect using the LIT under ambient conditions, eliminating the need for special sample surface preparation. Furthermore, compared with previous thermographic detection methods, the alternating thermal signal measured by the LIT is generated by the Peltier effect exclusively at the phase boundaries, making it spatially localized during the phase transition. In contrast to earlier passive thermographic inspection methods, this active LIT approach provides higher spatial resolution, greater sensitivity, and broader applicability for materials characterization. Here, we demonstrate the *in-situ* visualization of dynamically evolving phase boundaries in a dental rotary file under mechanical bending, whose complex surface morphology precludes a flat surface essential for optical probing, highlighting the LIT as a powerful, non-destructive tool for *in-situ* phase characterization in operational metallic materials. In addition, we image the phase boundaries of FeRh alloy, a material of significant interest in spintronics due to its potential for antiferromagnetic device applications[25–27]. Together, these results prove the generality of the method and underscore its potential to become a new paradigm for materials characterization.

2 Results

Figure 2a presents an infrared image of a NiTi wire in its austenite phase, exhibiting superelasticity at room temperature. We selected the NiTi alloy to demonstrate phase boundary visualization using the LIT due to its widespread applications and the ease with which martensite/austenite phase transitions can be induced by mechanical strain[28, 29]. In such transitions, the Peltier effect, as illustrated in Fig. 1b, is generated at the phase boundary when a charge current is applied[15, 16], because the Peltier coefficient of NiTi in the austenite phase differs from that in the martensite phase [24]. A symmetric bipolar square-wave charge current with a peak amplitude of $\pm$400 mA was applied to the NiTi wire. Due to the linear dependence of the Peltier effect on the current, the Peltier-induced signal reverses sign synchronously with the excitation and produces a thermal signal at the same frequency as the applied current, which is captured by the LIT to reveal the phase boundaries. The Joule heating, by contrast, scales with the square of the current and is therefore constant in time; it merely raises the steady-state temperature of the wire by a uniform offset, which—like the static thermal background of the non-conducting surroundings—is rejected by the lock-in detection (see Methods for details). A steady temperature increase of approximately 2 K across the wire is

induced by the alternating current due to the Joule heating, which only slightly modulates the mechanical properties of the NiTi wire[30]. Figure 2b displays the lock-in amplitude (A) and phase (ϕ) images obtained via the LIT for the NiTi wire shown in Fig. 2a. The absence of lock-in thermal signals indicates a uniform Peltier coefficient across the NiTi wire in its unstrained state.

Figure 2c shows the infrared image of the NiTi wire after undergoing mechanical bending, which led to substantial deformation. Figure 2d presents the corresponding LIT data for the bent NiTi wire shown in Fig. 2c, revealing a distinct pair of heating and cooling edges near the deformed region. The LIT amplitudes of both edges linearly scale with the applied current and their LIT phases are opposite to each other, as shown in Appendix Fig. A1, manifesting a typical behavior of the Peltier effect[16]. This "heating-cooling pair" pattern of the Peltier effect suggests a variation in the Peltier coefficient between the bent region and the rest of the sample, attributable to the formation of the martensite phase induced by plastic deformation in the NiTi alloy[31]. To verify that the LIT signal observed in Fig. 2d originates from the emergent martensite phase, we annealed the bent NiTi wire at 500 °C, a temperature known to effectively eliminate the martensite phase[32]. Figure 2e shows the infrared image of the annealed NiTi sample at room temperature, while Fig. 2f displays the corresponding LIT data, where the thermal pattern associated with the martensite phase disappeared. These findings corroborate the removal of the martensite phase through annealing, thereby strongly supporting phase boundary origin of the LIT signals observed in Fig. 2d. In addition, we performed complementary X-ray diffraction (Appendix Fig. A4) and latent-heat thermographic measurements (Supplemental Material, Movie S1)[33] on bent NiTi wires, both of which independently confirm the occurrence of the martensitic transition at the bent region. These cross-validations ensure the reliability of our conclusion.

Figure 3a illustrates NiTi wires coated with inks of different colors which were bent at room temperature. The three differently colored coatings are employed as a deliberate robustness test rather than a redundant repetition, spanning a representative range of emissivities and thicknesses (23 µm, 44 µm, and 40 µm for the black, red, and white coatings, respectively). Figures 3b–3d present the corresponding infrared images of these coated wires. The differences among these infrared images reflect the distinct thermal emissivities of the coatings within the detection wavelength range of the infrared camera (3–5 µm). Figures 3e–3g display the LIT data obtained using an alternating charge current of ±400 mA. The Peltier effect induced thermal pair patterns are clearly observed in the NiTi wires, similar to that in Fig. 2d, indicating the emergence of the martensite phase. Notably, the temperature amplitude of these patterns only slightly diminishes in the presence of a coating layer compared to that in Fig. 2d. Therefore, we successfully demonstrated the visualization of the strain-induced martensite/austenite phase transition in NiTi using the LIT under practical conditions, which shows unique robustness on oxidized or coated sample surfaces.

We can also employ the LIT to visualize the austenite/martensite phase transition in NiTi subjected to uniaxial stress[34]. Figure 4a shows the infrared image of a NiTi wire with a diameter of 0.15 mm used for this demonstration. Figure 4b illustrates the experimental setup, where both ends of the NiTi wire are fixed with opaque resin to a tensile machine that applies a stretching force to induce the reversible martensitic phase transition[29]. Figure 4c presents the strain-stress curve of the NiTi wire, which exhibits typical superelastic behavior [35]. Figures 4d–4o show the LIT images captured at selected points along the strain-stress curve. No LIT signal is detected before stress is applied, as seen in Fig. 4d. When the elongation (ΔL) reaches 0.4 mm, where the martensite phase transition is expected to occur according to the strain-stress curve, a pair of heating and cooling spots with opposite phases can be identified, as shown in Fig. 4e. Notably, the LIT signal in Fig. 4e was visible under a 0.5 mm thick resin layer, demonstrating the penetration advantage of infrared signal. We interpret the thermal pairs as the austenite/martensite phase boundaries since their appearance coincides with the onset of the martensitic phase transition in the stress-strain curve, which is similar to the results in Figs. 2 and 3.

The Peltier effect origin of the thermal pair is further confirmed by monitoring their displacement at higher ΔL, as shown in Figs. 4f–4j. As the NiTi wire is more stretched, the heating spot moves upwards and exits the field of view, while the cooling spot moves downwards and exits the field of view when the whole piece of NiTi becomes martensitic. The displacement of both spots is consistent with the well-known Lüders-band type movement of the phase boundary during the martensitic phase transition in NiTi, confirming that the two thermal spots mark the phase boundaries. When the stress is reduced, the NiTi wire gradually reverts to the austenite phase, and the heating and cooling spots reappear and move towards each other, as seen in Figs. 4j–4o. Finally, the NiTi wire returns to its initial austenite phase with no detectable LIT signal. Appendix Fig. A2 shows the same measurement as in Fig. 4 for a pre-bent NiTi wire, where the martensitic phase forms first at the pre-bent position due to the maximized strain under stress. It is observed that the heating and cooling pair spots emerge from the pre-bent position and exhibit typical Lüders-band type behavior as in Fig. 4b, reconfirming the validity of the LIT for phase boundary visualization via the Peltier effect.

We employ the LIT to visualize the martensitic phase transition in a dental rotary file, which is made of a NiTi alloy and is widely used in root canal retreatment[36]. Figure 5a shows the infrared image and the LIT data of the dental rotary file in the unstrained state, where no phase boundary was observed. Figure 5b illustrates the experimental setup designed to simulate the working conditions of the dental rotary file, where the file tip was stuck into a fissure on a tooth model. The dental rotary file can be bent by controlling the linear motion stage that holds the rotary handpiece. Figures 5c–5h display infrared images and the corresponding LIT data for the dental rotary file during a

bending cycle. The thermal pair pattern was once more observed, and the distance between the heating and cooling edges synchronized with the strain generated in the file. This behavior is consistent with the expected martensitic phase transition in NiTi, effectively outlining the phase boundaries. It is worth noting that the surface of a dental rotary file has a complex structure, which precludes spatial phase resolution by conventional methods, especially in an ambient environment. Here, a matte black paint was sprayed onto the file, which yields a high and nearly Lambertian emissivity, i.e., the observed thermal radiance of a Lambertian surface is virtually independent of the viewing angle. In addition, the depth of field of our imaging system (± 0.12 mm) exceeds the surface relief at the file tip (~ 0.1 mm), so the entire faceted surface remains in focus and defocus blurring is negligible. These conditions together preserve the spatial resolution across the undulating geometry, allowing the phase boundaries to be clearly resolved. Therefore, the LIT method has a unique advantage for imaging the phase distribution in phase-transition materials in service with complex shapes, such as coronary stents, biopsy forceps, retrieval baskets and aneurysm clips[37–39].

Finally, to demonstrate the general applicability of the LIT method in resolving phase boundaries, we present experimental results in FeRh, which undergoes a structural phase transition around $360\,\mathrm{K}$[40–42]. FeRh exhibits antiferromagnetism (AFM) below the transition temperature and ferromagnetism (FM) above the transition temperature. A $50\,\mathrm{nm}$ FeRh film was epitaxially grown on a $MgAl_2O_4$ substrate by sputtering and patterned into a cross-shaped strip with a width of $100\,\mu\mathrm{m}$. The temperature dependence of the FeRh resistance is shown in Fig. 6a, indicating an FM phase above $370\,\mathrm{K}$ and an AFM phase below $340\,\mathrm{K}$[25, 43–45]. Notably, within the intermediate temperature range of $340\,\mathrm{K}$ to $370\,\mathrm{K}$, a pronounced hysteresis loop emerges, signifying the coexistence of FM and AFM phases—a hallmark of a first-order phase transition[46].

The experimental setup is illustrated in Fig. 6b, and the infrared image of the sample is shown in Fig. 6c. The horizontal strip was connected to a tunable DC power supply, while the vertical strip was connected to the LIT excitation signal. Initially, the sample was cooled below $340\,\mathrm{K}$ and then reheated to $360\,\mathrm{K}$ to place it within the two-phase coexistence temperature window while remaining entirely in the AFM state (corresponding to state A in Fig. 6b). The absence of an LIT signal in both the amplitude and phase images (Fig. 6d) is consistent with the expectation of no phase boundary.

Subsequently, a $120\,\mathrm{ms}$ voltage pulse was applied to the horizontal strip. The Joule heating induced by the current can raise the temperature of the horizontal strip above 370 K (corresponding to state B in Fig. 6b), triggering the phase transition. Upon subsequent cooling to $360\,\mathrm{K}$, the horizontal strip remained in the FM state, corresponding to state C in Fig. 6b. As a result, phase boundaries emerged in the vertical strip. The LIT data, which reveal two phase boundaries characterized by paired Peltier heating and cooling spots with opposite phase signals, are shown in Fig.

6e and are consistent with this expectation. Moreover, as shown in Figs. 6f-6k, when the heating power increases with elevated voltage, the phase-transition region drives the phase boundaries to propagate along the vertical strip. The ability to image phase boundaries in FeRh as readily as in NiTi highlights the universality of the LIT as a method for phase boundary characterization.

3 Discussion

In this work, we demonstrated a versatile, in-situ, and non-destructive technique that resolves phase boundaries in metallic materials by detecting the localized Peltier effect [24, 47, 48]. Owing to the high temperature resolution of the LIT [23], we were able to extract the weak, AC-modulated heating–cooling signal originating from the boundary region with an inhomogeneous Peltier coefficient, and thereby reveal the spatial distribution of these boundaries in NiTi [49, 50] and FeRh [41, 51]. Unlike conventional imaging tools—such as electron and optical microscopy, which require flat, clean surfaces and often a high-vacuum environment far from service conditions—the LIT operates directly under service conditions in ambient air. Moreover, because the underlying thermal wave can effectively propagate through thin dielectric layers [23], it tolerates native oxide and opaque coatings and remains robust on surfaces of complex geometry. By utilizing lenses of different magnification, the LIT enables the inspection of phase transitions and material failures across a wide range of length scales, from centimeters to micrometers [52], providing valuable insights into the mesoscopic mechanisms of both functional and structural materials. Therefore, this technique offers a promising route toward the in-situ characterization of phase-transforming metallic materials operating under service conditions, opening opportunities in structural health monitoring and failure analysis [53].

The absolute value of the LIT signal depends on multiple coupled factors—the thermoelectric properties of the material, the local current density distribution, the surface emissivity, and convective heat exchange with the surroundings [23, 47]. Precisely measuring these parameters and performing the accompanying coupled thermoelectric finite-element modeling remain challenging, so a fully quantitative analysis is left for future work. Nevertheless, the LIT method already introduces a powerful new dimension to materials analysis. When cross-correlated with established techniques such as EBSD, XRD, and DSC, it enables comprehensive multi-modal characterization of phase transformations [49, 51]. Ultimately, by generating massive, rich thermal datasets, the LIT holds the potential to complement existing modalities and drive fast, accurate materials characterization in data-driven and AI-powered research contexts [54].

Methods

Sample preparation The NiTi alloy wires used in Fig. 2 and Fig. 3 were commercial NiTi wires with a diameter of $0.6\,\mathrm{mm}$. The alloy composition consists of approximately 54% nickel and 46% titanium by weight. The coating layers of NiTi wires shown in Fig. 3 included black, red, and white paint. The average thicknesses of the black, red, and white coatings were measured using a micrometer to be $23\,\mu\mathrm{m}$, $44\,\mu\mathrm{m}$, and $40\,\mu\mathrm{m}$, respectively. For the annealing process, the NiTi alloy wires of Fig. 2 were placed in a muffle furnace. The temperature was increased from $50\,^{\circ}\mathrm{C}$ to $500\,^{\circ}\mathrm{C}$ at a rate of $5\,^{\circ}\mathrm{C}$ per minute and maintained at $500\,^{\circ}\mathrm{C}$ for 2 hours. The dental NiTi rotary file of Fig. 5 was sourced from Shenzhen Flydent Medical Co., Ltd. The specific model used was a $25\,\mathrm{mm}$ 15# NiTi file, commonly used in dental applications for root canal procedures.

Experiment setup All samples were fixed during measurement to ensure no displacement, thereby maintaining signal stability throughout the measurement process. For the NiTi rotary file sample shown in Fig. 5, one end was fixed on a horizontal dovetail linear displacement stage, while the other end was in contact with the tooth model. The bending degree of the NiTi rotary file was controlled by adjusting the movement of the displacement stage. In all the measurements, the contacts for applying current are far from the LIT viewing area, eliminating the parasitic electric-thermal signals.

Lock-in thermography (LIT) measurement The LIT measurements (except for Fig. 4, Fig. 6, and Appendix Fig. A2) were conducted using the Thermo100 system (Anhui Luxet Infrared Technology Co.), while the LIT data in Fig. 4, Fig. 6, and Appendix Fig. A2 were acquired using the ImageIR 8300-hpd (InfraTec GmbH). All measurements were performed at room temperature and atmospheric pressure. The LIT system consists of three main components: a measurement source unit, infrared thermography, and a lock-in calculation module. A periodic square wave current (in constant current mode, with a zero DC component, ensuring constant Joule heating) was applied to the sample under test by the measurement source unit. The sample then generated a corresponding periodic thermal response. The temperature distribution on the sample was continuously recorded using infrared thermography ($100\,\mathrm{Hz}$ frame rate). The lock-in calculation module was subsequently applied to the acquired infrared images, enabling the extraction of amplitude and phase information of the modulated thermal response in terms of its spatial distribution. The amplitude image reveals the locations where the temperature responds to the periodic modulation, while the phase image provides the phase delay of the temperature response. If the AC temperature signal of a region is in-phase with the applied current, it means heating effect. Conversely, if the AC temperature signal is in opposite phase to the current, it is cooling effect.

Separation of Joule and Peltier contributions In the LIT measurement, two dominant contributions are mixed together in the thermal response: Joule heating and the Peltier effect. Under ideal conditions, the Joule heating depends on the square of the current; because the symmetric bipolar square-wave current applied to the sample has zero DC component ($I_+ = -I_-$), I^2 is constant at every instant, so the Joule heating is time-independent and produces only a steady (DC) temperature offset. In contrast, the Peltier signal, being linear in I, alternates sign synchronously with the current and constitutes the modulated thermal response detected at the lock-in reference frequency f. Regardless of its magnitude, the Joule heating thus contributes nothing at f, while only the modulated Peltier component survives the lock-in demodulation. In practice, however, the Joule heating can still affect the LIT result under non-ideal conditions. Below we list the possible channels through which this contamination arises, together with the measures we take to avoid them:

(i) *Asymmetric current waveform.* Rigorous cancellation of the Joule contribution at the lock-in frequency requires the square-wave excitation to satisfy $I_+ = -I_-$; an amplitude asymmetry $I_+ + I_- \neq 0$, arising for example from a non-ideal current source or from asymmetric contact resistances, would give I^2 a non-zero component at f that is indistinguishable from a genuine Peltier signal. In our setup the excitation was supplied by a Keithley Model 2612A SourceMeter, which delivers the $400\,\mathrm{mA}$ drive current with a specified output accuracy of $\pm 0.2\,\mathrm{mA}$; we further verified before each measurement, by monitoring the voltage across the sample with an oscilloscope, that the residual DC offset of the sample current was indistinguishable from the oscilloscope noise floor.

(ii) *Measurement before the average temperature reaches steady state.* When the current is first switched on, the bulk temperature of the sample rises on a thermal time constant $\tau_{\mathrm{th}} = C_{\mathrm{th}}/G_{\mathrm{th}}$ set by the heat capacity and the heat-loss conductance to the environment. During this transient, the temperature drift is not constant in time, and its slowly-varying Fourier tail bleeds into the lock-in ω band, contaminating the Peltier amplitude with a systematic bias[23]. We therefore begin the LIT measurement only after the average-temperature plateau of the sample has been reached (typically several minutes after current onset, monitored continuously by the IR camera).

(iii) *Excessive current density perturbing the phase distribution.* Although Joule heating contributes no AC signal, it raises the steady-state sample temperature; if this rise becomes comparable to the gap between the operating temperature and the transformation temperature, the measurement itself would shift or erase the phase distribution. For the NiTi wires we restricted the current to values producing a steady-state temperature rise of about $2\,\mathrm{K}$, well below the gap to the austenite-finish temperature, and for the FeRh film we stayed far from the AFM/FM transition temperature, so that the chosen current level does not by itself trigger a phase transition.

Spatial resolution of the LIT The optical spatial resolution Δx of the LIT is fundamentally limited by the diffraction of the detected infrared wavelength, which can be approximated by $\Delta x \sim 1.22\frac{\lambda f}{D}$, where λ is the detected wavelength, f is the focal length of the thermal camera lens, and D is the aperture diameter of the lens[55, 56]. In our system, the optical resolution is around $2\,\mu\mathrm{m}$.

The dispersion of the lock-in signal due to thermal diffusion also imposes an important constraint. A shorter thermal diffusion length indicates a more localized thermal signal, which in turn leads to improved spatial resolution for detecting phase boundaries. For clarity, we consider the one-dimensional case of heat conduction in an isotropic and homogeneous medium. The governing heat conduction equation is

$$c_p\rho\frac{\partial T}{\partial t} = \kappa\frac{\partial^2 T}{\partial x^2}$$

, where T is the temperature, t is time, c_p is the specific heat, ρ is the density, and κ is the thermal conductivity. The solution of this equation takes the form:

$$T = A\exp\left(-\frac{x}{\Lambda}\right)\exp\left(i(\omega t - \frac{x}{\Lambda})\right)$$

, where $\Lambda = \sqrt{\frac{2\kappa}{\rho c_p \omega}}$ is the so-called thermal diffusion length which can characterize the resolution of the LIT[23]. Clearly, for fixed material parameters (ρ,c_p,κ), Λ can be reduced by increasing the lock-in frequency ω. However, higher excitation frequencies are constrained, first by the Nyquist sampling theorem-where the maximum usable lock-in frequency is one-quarter of the infrared camera frame rate-and second by the reduction in modulated thermal signal amplitude as the lock-in frequency increases under constant electrical excitation amplitude. Therefore, an appropriate trade-off among multiple measurement parameters is required. For our measurements at $\omega = 2\pi \times 25\,\mathrm{Hz}$, and taking the thermal diffusion $\frac{\kappa}{\rho c_p} = 4.17\,\mathrm{mm}^2/\mathrm{s}$ for the NiTi alloy (The average thermal diffusivity of austenitic and martensitic Nitinol)[57], we obtain $\Lambda \approx 230\,\mu\mathrm{m}$. This value is comparable to the half-peak width (around $160\,\mu\mathrm{m}$) of our experimental data shown in Appendix Fig. A3 (based on the same raw data as Fig. 2 in the manuscript). The spatial resolution of the LIT is therefore sufficient to meet the requirements of most macroscopic applications, e.g. the dental rotary file.

The noise level of the LIT The amplitude level of noise can be theoretically expressed as

$$\langle A_{\mathrm{noise}}\rangle = \frac{2}{\sqrt{f_{\mathrm{frame}} t_{\mathrm{acq}}}}\mathrm{NETD}$$

, where t_{acq} is the acquisition time, f_{frame} is the frame rate of the thermal camera, and the noise equivalent temperature difference(NETD) quantifies the noise level of the infrared camera focal plane array (FPA)[23]. There are several strategies to reduce $\langle A_{\mathrm{noise}}\rangle$. On the one hand, increasing t_{acq} or raising f_{frame} (by activating only part pixels

of the FPA) can effectively suppress noise. On the other hand, employing a mid-wave infrared (MWIR) camera with a cooled FPA detector can further suppress the thermally induced dark current and thereby improve the NETD.

In our measurements, we used an infrared camera whose FPA was operated at approximately $80\,\mathrm{K}$, with a frame rate of $f_{\mathrm{frame}} = 100\,\mathrm{Hz}$, and the acquisition time was set to $t_{\mathrm{acq}} = 80\,\mathrm{s}$. The standard deviation of the background signal was below $0.2\,\mathrm{mK}$, more than an order of magnitude smaller than the measured thermal signal of $\sim 4\,\mathrm{mK}$, thereby ensuring the reliability and quality of the experimental data.

Acknowledgements

D.H. was supported by the USTC Center for Micro- and Nanoscale Research and Fabrication. Part of the work was carried out at the Instruments Center for Physical Science, University of Science and Technology of China. K.U. was supported by CREST "Creation of Innovative Core Technologies for Nano-enabled Thermal Management" (JPMJCR17I1) and ERATO "Magnetic Thermal Management Materials" (JPMJER2201) from JST, Japan; Grant-in-Aid for Scientific Research (S) (22H04965) from JSPS, Japan; and NEC Corporation.

Declarations

Author contributions D.H. and K.U. designed the experiment, J.Z.,P.T., F.Z. and D.H. prepared the samples. J.Z., T.H. and D.H. performed the measurement and collected all of the data. T.H., R.I., K.U., D.H., J.Z., X.C. and C.S.analyzed the data. All the authors discussed the results and prepared the manuscript.

Competing Interests The authors declare that they have no competing financial interests.

Data Availability There are no publicly available research data or software supporting this manuscript. Requests for further information or data should be sent to the authors.

Correspondence Correspondence and requests for materials should be addressed to D.H. (email: dazhi@ustc.edu.cn).

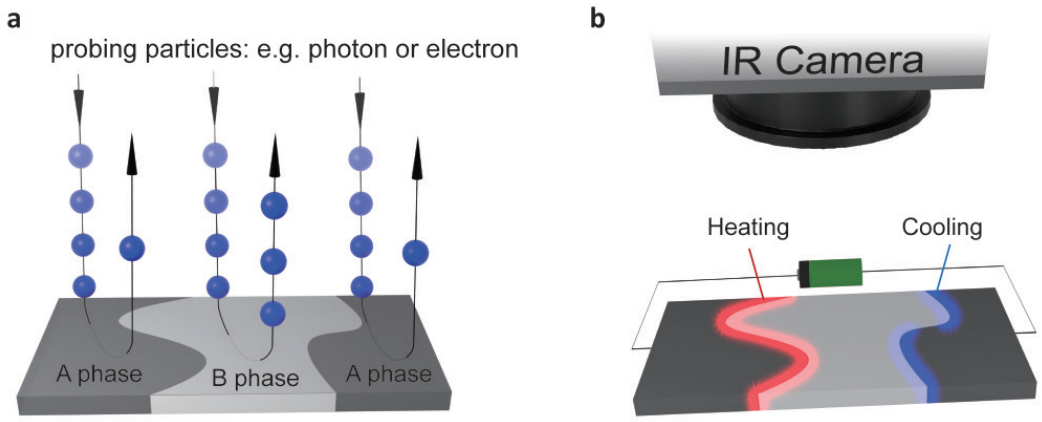


Fig. 1 Comparison of phase boundary resolution using lock-in thermography and conventional methods. a. Conventional techniques for resolving phase boundaries utilizing photons or electrons as probes. The phase boundary is determined through optical contrast, which arises from the differing reflection rates of incident particles on different phases. **b**. Lock-in thermography method for resolving phase boundaries. An alternating charge current is applied through the sample, inducing periodic temperature modulation at the phase boundaries via the Peltier effect. This effect, caused by different Peltier coefficients in adjacent phases, reveals the phase boundary profile in the thermal image.

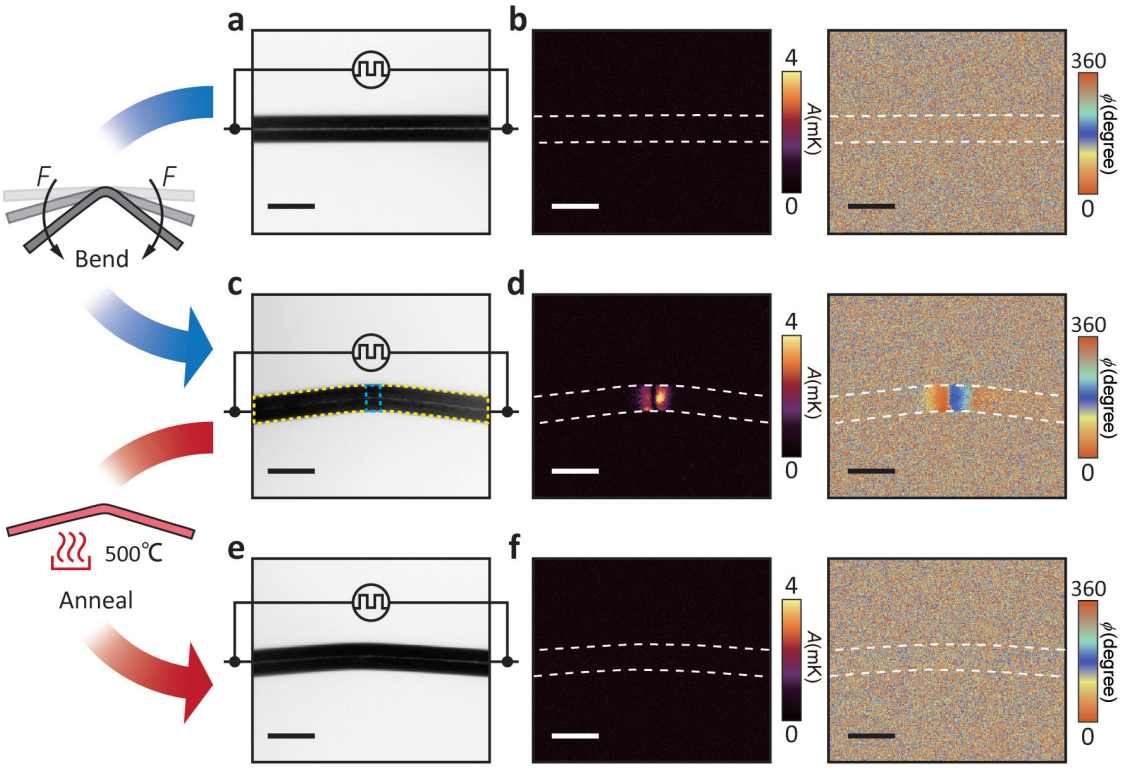


Fig. 2 Lock-in thermography imaging of phase separation in a bent NiTi wire. a. Infrared photograph of a 0.6-mm-diameter superelastic NiTi wire with a natural oxidation layer at room temperature. An alternating charge current of 400 mA is applied to the NiTi wire to induce the Peltier effect at phase boundaries, if present. The scale bar length is 1 mm. **b**. Lock-in amplitude (A) and phase (ϕ) images of the NiTi wire shown in Fig. 2a. The profile of the NiTi wire is indicated by dashed lines. The absence of the Peltier effect suggests that the NiTi wire is in a uniform austenite phase. **c-d**. Infrared photograph of the NiTi wire after mechanical bending and the corresponding lock-in amplitude and phase images measured under an alternating charge current of 400 mA. A pair of heating and cooling edges due to the Peltier effect near the deformed region of the NiTi wire are observed in the LIT images, visualizing the boundaries between the parent austenite phase and the bending-induced martensite phase. Guided by the phase boundary determined by the LIT, the austenite and martensite regions are contoured in yellow and blue, respectively, in Fig. 2c. **e-f**. Infrared photograph of the bent NiTi wire after annealing at 500 °C and the corresponding lock-in amplitude and phase images measured under an alternating charge current of 400 mA. The disappearance of the Peltier effect indicates that the bending-induced martensite phase has reverted to the austenite phase due to annealing.

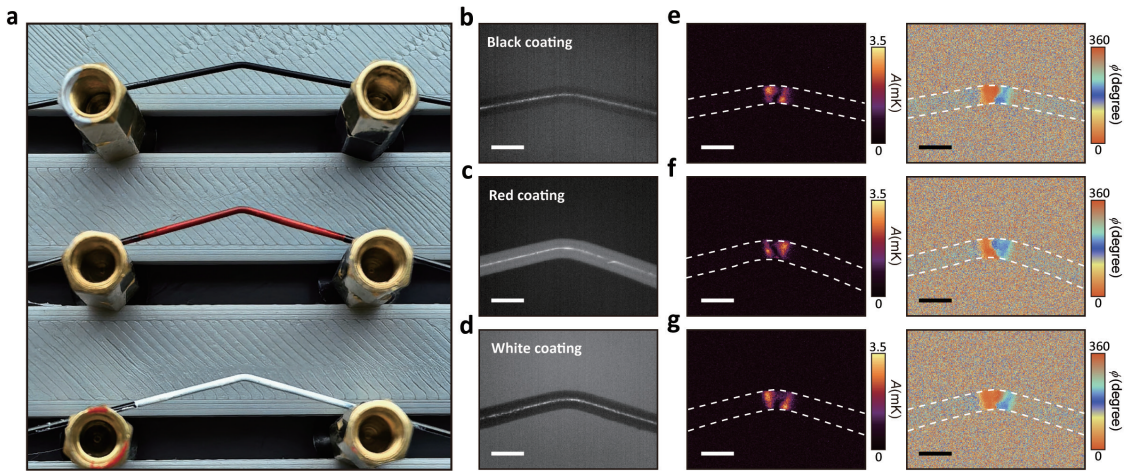


Fig. 3 Lock-in thermography imaging of phase separation in bent NiTi wires with opaque coating layers. a. Visible-light photographs of three bent NiTi wires with different coating layers. **b-d**. Infrared photographs of the three bent NiTi wires shown in Fig. 3a. **e-g**. Lock-in amplitude and phase images of the bent NiTi wires shown in Figs. 3b, 3c, and 3d, respectively. Similar thermal patterns induced by the Peltier effect at the phase boundaries are observed. The profile of each NiTi wire is indicated by dashed lines.

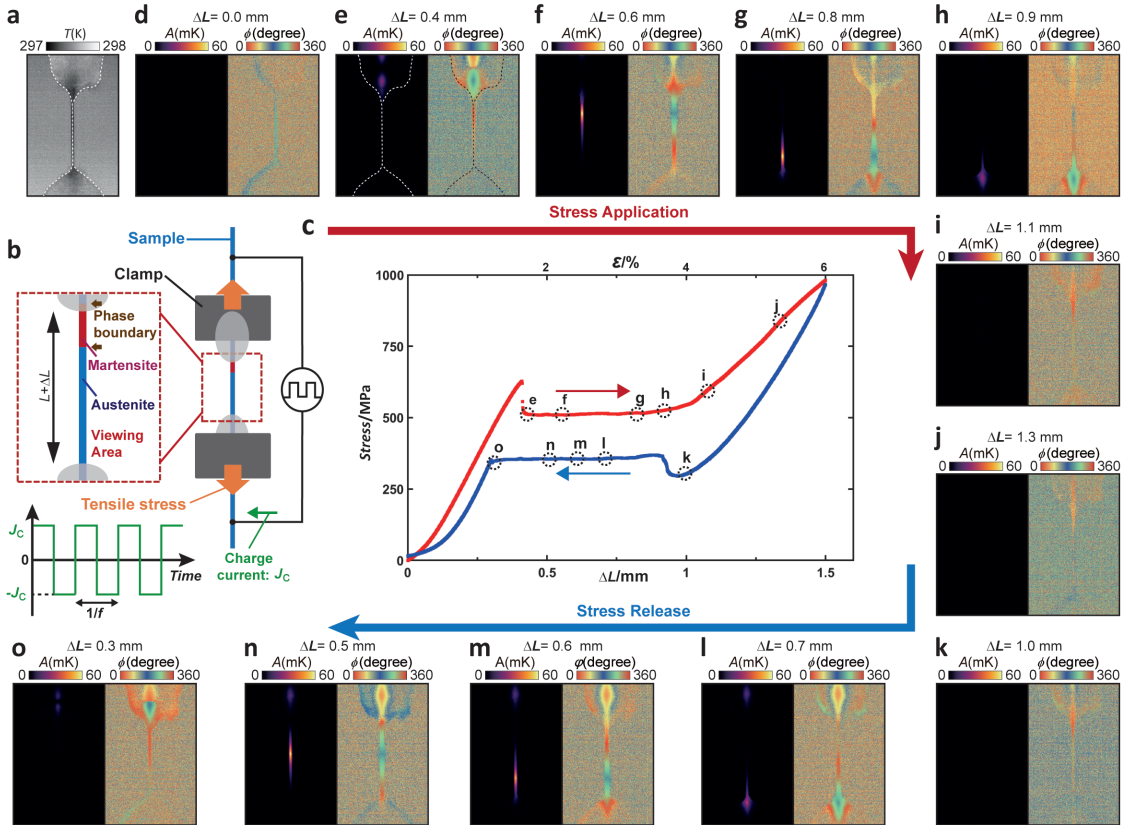


Fig. 4 Lock-in thermography imaging of stress-induced martensitic phase transition in a NiTi wire. a. Infrared image of the NiTi wire fixed on a tensile testing machine. **b**. Schematic of the experimental setup for the LIT imaging of stress-induced martensitic transformation in a NiTi wire. The NiTi wire is stretched using a tensile machine, with its length and applied stress monitored simultaneously. **c**. Stress-strain curve of the NiTi wire during a superelastic transformation cycle. **d-o**. Lock-in amplitude and phase images at selected points on the stress-strain curve, as indicated in Fig. 4c. Austenite/martensite phase boundaries are resolved through Peltier-effect-induced heating and cooling spots.

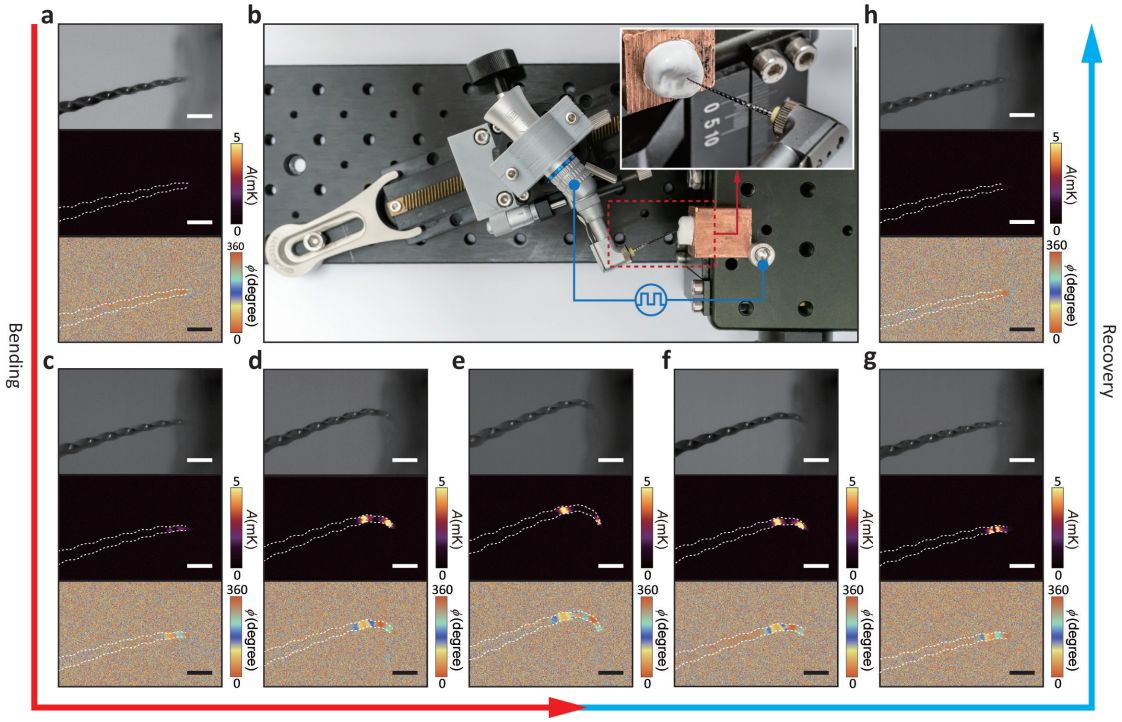


Fig. 5 Lock-in thermography imaging of strain-induced martensitic phase transition in a dental rotary file. a. Infrared image, lock-in amplitude, and phase images of the dental rotary file in the initial unstrained state. **b**. Visible-light photograph of the dental rotary file and the experimental setup. **c-h**. Infrared images, lock-in amplitude, and phase images of the dental rotary file during mechanical bending against a tooth model, which simulates the working conditions in clinical applications. The emergence and disappearance of phase boundaries are clearly captured via the Peltier effect in the LIT images, enabling visualization of the phase transition in the dental rotary file.

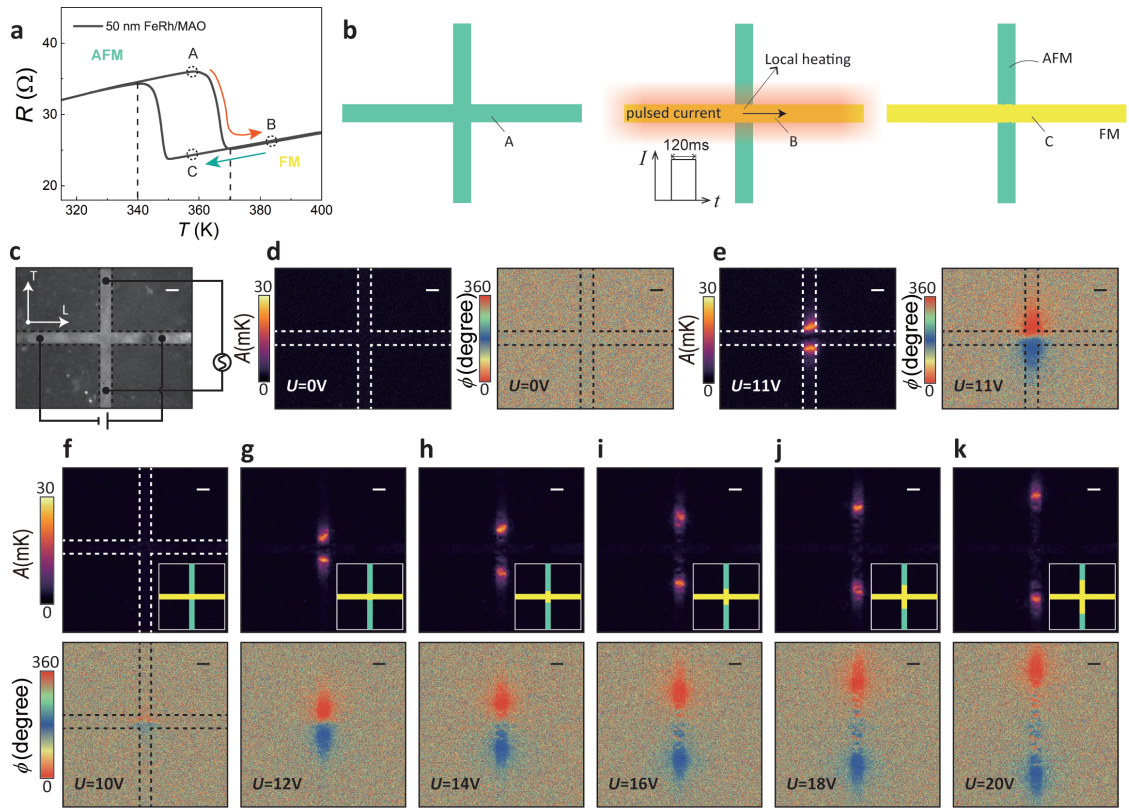


Fig. 6 Lock-in thermography imaging of the heating-induced AFM-FM transition in FeRh alloy. a. Temperature dependence of the resistance of FeRh, showing a pronounced thermal hysteresis. **b**. Schematic illustration of the phase distribution in the sample. Joule heating drives the horizontal AFM strip into the FM state; points A, B, and C correspond to the dashed circles indicated in Fig. 6a. **c**. Infrared image of the cross-shaped FeRh sample. **d**. Lock-in amplitude and phase images of FeRh without phase boundaries (state A in Fig. 6b), which was taken before the pulse voltage application. **e**. Lock-in amplitude and phase images of FeRh, showing clear AFM/FM phase boundaries (state C in Fig. 6b) after the application of an 11 V voltage pulse, were resolved through Peltier-effect-induced heating and cooling spots. **f-k**. Lock-in amplitude and phase images of the FeRh sample under increasing heating power. The progressively separated heating and cooling spots indicate that the phase boundary propagates along the vertical strip as the heating power increases.

Appendix

To confirm that the measured experimental data primarily arise from the Peltier effect at the phase boundaries, we analyzed the relationship between the amplitude of the LIT signal at the phase boundaries and the applied current. As shown in Fig. A1b, the red and blue circles denote the average amplitude values within region 1 and region 2 (marked in Fig. A1a), respectively. Linear fitting results, represented by dashed lines, indicate that the amplitude of the LIT signal is approximately proportional to the applied current. Moreover, the average phase values of the LIT signal in these two regions remain nearly constant with respect to the applied current, as shown in Fig. A1d. Notably, they exhibit a 180° phase difference, consistent with the expected heating and cooling effects at the respective phase boundaries. These observations validate the reliability of the LIT data and support the dominance of the Peltier effect in the measured response.

Figure A2 illustrates the tensile process of a pre-bent sample. Figures A2a and A2c present the infrared image and the corresponding LIT data of the pre-bent sample, where phase boundaries have already formed. Figures A2c– A2f show the LIT images during the tensile process. Due to the defect introduced by the bending operation, significant stress accumulated at the pre-bent position during stretching. Consequently, the martensitic phase initiated at the pre-bent position and progressively expanded during the tensile process.

Figure A3 analyzes the spatial resolution of the LIT, determined by thermal diffusion, at a lock-in frequency of 25 Hz. Figure A3a shows the LIT amplitude image of the bent NiTi wire, derived from the same raw data as Fig. 2d. The profile line data in Figure A3b are extracted from the white dashed line in Figure A3a. The calculated half-peak widths of the two peaks are $139\,\mu\mathrm{m}$ and $161\,\mu\mathrm{m}$, respectively. The mutual compensation of heating and cooling suppresses spatial diffusion of the modulated thermal signal, leading to half-peak widths slightly smaller than the theoretical values calculated in the Methods section.

To independently corroborate the bending-induced austenite-to-martensite transition, we performed X-ray diffraction (XRD) measurements on bent NiTi wires, as shown in Fig. A4. The investigated samples were Ni-rich superelastic medical-grade NiTi alloy wires (55.4 wt% Ni) with a diameter of $1\,\mathrm{mm}$. To enhance the XRD signal, four NiTi wires bent to the same angle were tightly bundled together and mechanically polished to obtain a flat, mirror-like surface. We then performed 2θ line scans on both the bent and unbent regions (Areas 1 and 2 in Fig. A4a), and the resulting profiles are shown in Fig. A4b. The peak at around 42.5° corresponds to the austenite phase (B2), while the shoulder near 40° is characteristic of the martensite phase (B19′). Compared with the unbent region, the profile of the bent region exhibits an enhanced B19′ signal accompanied by a reduced B2 signal, indicating an increased

martensite phase fraction and thereby providing direct structural evidence that bending locally induces martensite formation, in full agreement with the LIT signal observed in Fig. 2d.

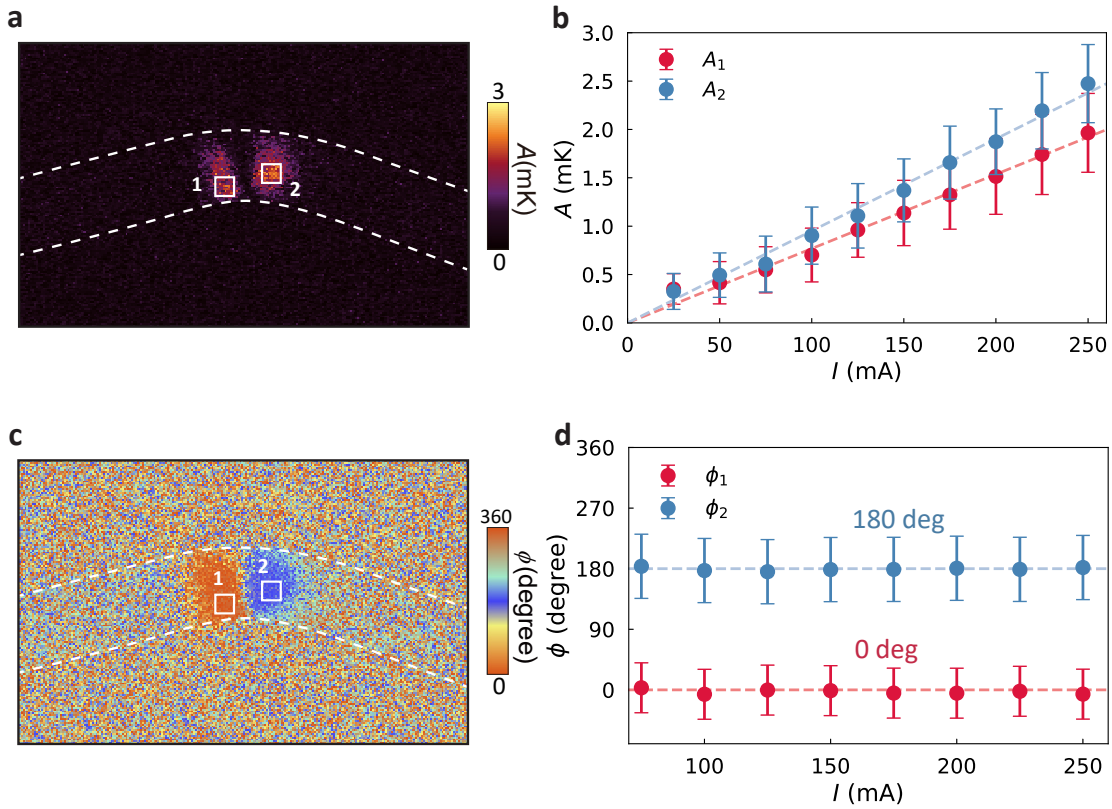


Fig. A1 Dependence of the amplitude and phase of the LIT signal on the applied current. a. The amplitude image at 200 mA applied current. The squares mark the regions where amplitude values were averaged for quantitative analysis. **b**. Plot of the LIT signal amplitude versus applied current. The data points were fitted with a linear function, indicating a proportional relationship between the LIT signal amplitude and the applied current. **c**. Corresponding phase image at 200 mA applied current. The squares mark the regions where phase values were averaged for quantitative analysis. **d**. Plot of the LIT signal phase versus applied current. The average phase values keep nearly constant with respect to the applied current, and exhibit a 180° phase difference.

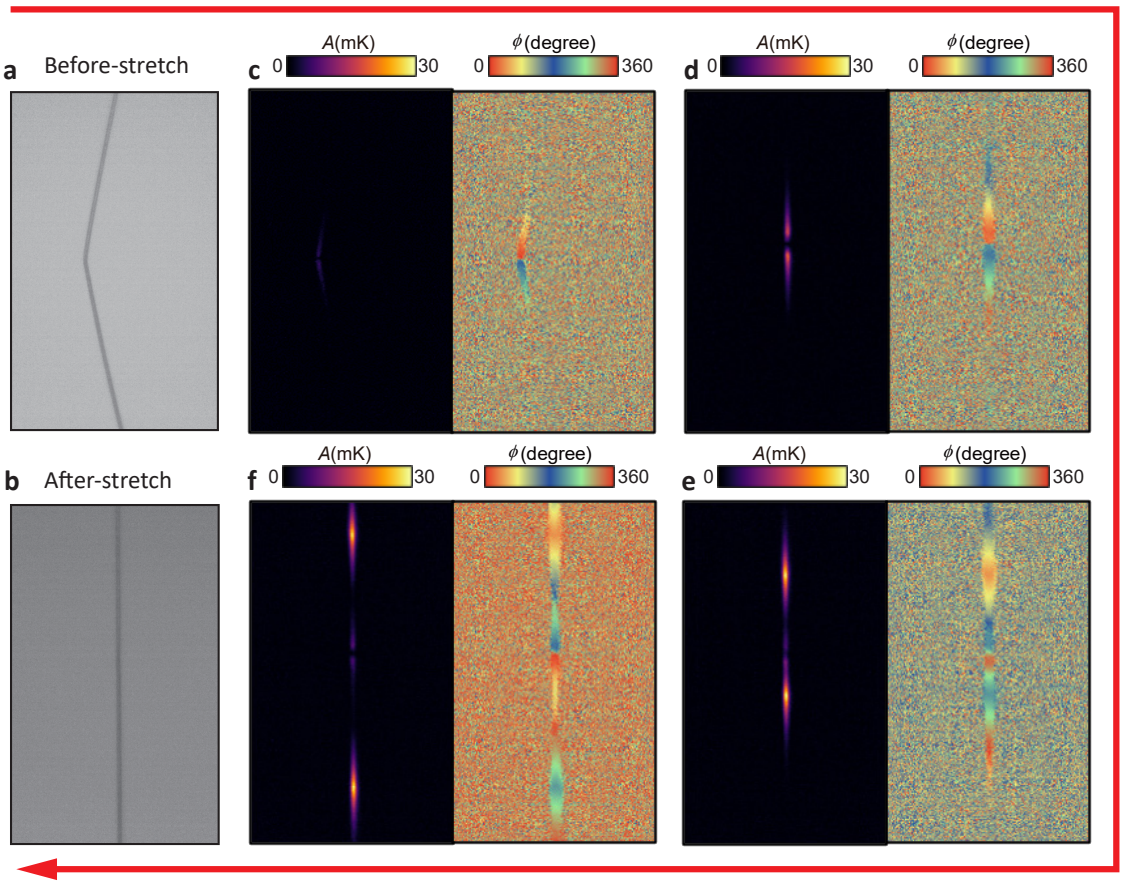


Fig. A2 Lock-in thermography imaging of stress-induced martensitic phase transition in a pre-bent NiTi wire. a. Infrared image of the pre-bent NiTi wire before stretching. **b**. Infrared image of the pre-bent NiTi wire after stretching. **c-f**. Lock-in amplitude and phase images of the pre-bent NiTi wire during stretching. The martensitic phases initiated at the pre-bent position and progressively expanded during the tensile process.

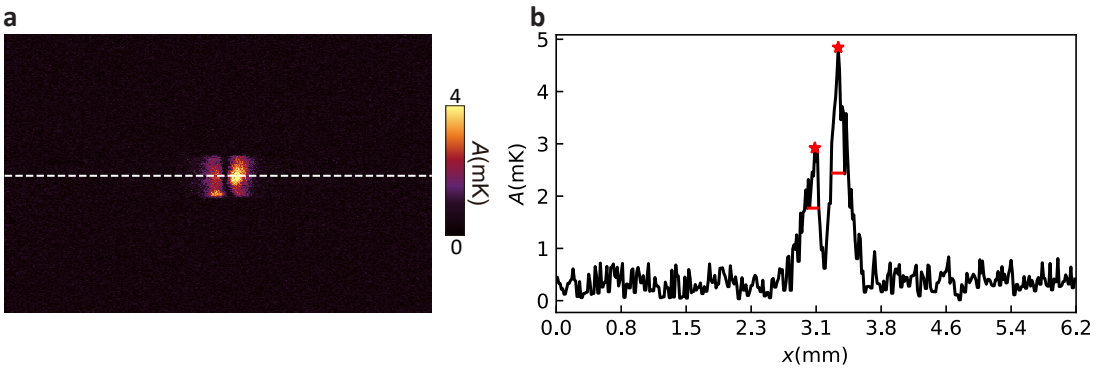


Fig. A3 Resolution analysis for Lock-in thermography. a. Amplitude image of the LIT data for a NiTi alloy wire at a lock-in frequency of 25 Hz (based on the same raw data as Fig. 2d). **b**. Profile line corresponding to the white dashed line in panel **a**; the red short line indicates the half-peak width.

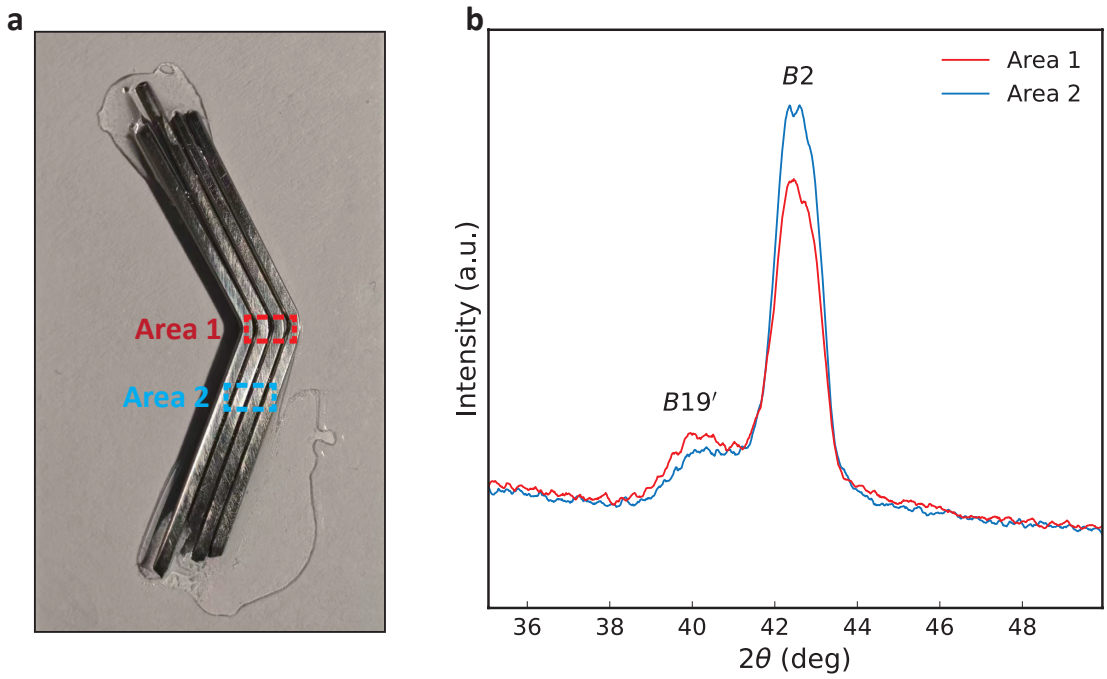


Fig. A4 X-ray diffraction characterization of the bending-induced martensite formation in NiTi wires. a. Photograph of four NiTi wires bent to the same angle and tightly bundled together to enhance the XRD signal. Area 1 (red) is located at the bent region and Area 2 (blue) at the unbent region, corresponding to the two profiles in panel **b**. **b**. XRD 2θ line-scan profiles measured on the bent (Area 1, red) and unbent (Area 2, blue) regions. The peak at around $42.5°$ corresponds to the austenite phase (B2), while the shoulder near $40°$ is characteristic of the martensite phase (B19′). Compared with the unbent region, the bent region exhibits an enhanced B19′ signal accompanied by a reduced B2 signal, indicating an increased martensite phase fraction induced by bending.

References

[1] V. A. Somenkov and S. S. Shil'stein, Prog. Mater. Sci. **24**, 267 (1980).

[2] A. L. Roitburd, in *Solid State Physics*, Vol. 33, edited by H. Ehrenreich, F. Seitz, and D. Turnbull (Academic Press, 1978) pp. 317–390.

[3] S. A. Shabalovskaya, Bio-Med. Mater. Eng. **6**, 267 (1996).

[4] E. David, J. Mater. Process. Technol. **162–163**, 169 (2005).

[5] M. Wuttig and N. Yamada, Nat. Mater. **6**, 824 (2007).

[6] I. Sarbu and C. Sebarchievici, Sustainability **10**, 191 (2018).

[7] T. Waitz, V. Kazykhanov, and H. Karnthaler, Acta Mater. **52**, 137 (2004).

[8] P. Sedmák, J. Pilch, L. Heller, J. Kopeček, J. Wright, P. Sedlák, M. Frost, and P. Šittner, Science **353**, 559 (2016).

[9] W. Tu, S. Zhong, M. Luo, and Q. Zhang, Front. Phys. **9**, 676851 (2021).

[10] R. Wu, H. Zhang, R. Yang, W. Chen, and G. Chen, J. Sens. **2021**, 6640406 (2021).

[11] Y. S. Choi, J. G. Kim, Y. S. Kim, and J. Y. Huh, Int. J. Automot. Technol. **9**, 625 (2008).

[12] C. Mailhé, A. Godin, A. Veillère, and M. Duquesne, Appl. Sci.-Basel **11**, 8885 (2021).

[13] D. Delpueyo, X. Balandraud, and M. Grédiac, Mater. Sci. Eng. A-Struct. Mater. Prop. Microstruct. Process. **528**, 8249 (2011).

[14] J. Chen, Q. Zhang, B. Wei, W. Wang, W. Zhang, L. Lei, U. Ramamurty, and G. Fang, J. Mater. Sci. Technol. **226**, 158 (2025).

[15] J. C. A. Peltier, Ann. Chim. Phys. **56**, 371 (1834).

[16] T. M. Tritt, in *Encyclopedia of Materials: Science and Technology* (Elsevier, 2002) pp. 1–11.

[17] K. Nakagawa, T. Yokouchi, and Y. Shiomi, Sci. Rep. **11**, 24216 (2021).

[18] K. Uchida, T. Hirai, F. Ando, and H. Sepehri-Amin, Adv. Energy Mater. **14**, 2302375 (2024).

[19] T. Hirai, F. Ando, H. Sepehri-Amin, and K. Uchida, Nat. Commun. **15**, 9643 (2024).

[20] T. Favaloro, J. Suh, B. Vermeersch, K. Liu, Y. Gu, L.-Q. Chen, K. X. Wang, J. Wu, and A. Shakouri, Nano Lett. **14**, 2394 (2014).

[21] J. Lee, G. McIntosh, A. Kaiser, Y. Park, M. Kaack, J. Pelzl, C. K. Kim, and K. Nahm, J. Appl. Phys. **89**, 6223 (2001).

[22] Y. Kimura, K. Utsumi, and H. Tohmyoh, Appl. Therm. Eng. **255**, 124009 (2024).

[23] O. Breitenstein, W. Warta, and M. Langenkamp, *Lock-in thermography: basics and use for evaluating electronic devices and materials*, 2nd ed. (Springer, 2010).

[24] K. Uchida, S. Daimon, R. Iguchi, and E. Saitoh, Nature **558**, 95 (2018).

[25] X. Marti, I. Fina, C. Frontera, J. Liu, P. Wadley, Q. He, R. Paull, J. Clarkson, J. Kudrnovskỳ, I. Turek, *et al.*, Nat. Mater. **13**, 367 (2014).

[26] V. Baltz, A. Manchon, M. Tsoi, T. Moriyama, T. Ono, and Y. Tserkovnyak, Rev. Mod. Phys. **90**, 015005 (2018).

[27] Y. Wang, M. M. Decker, T. N. Meier, X. Chen, C. Song, T. Grünbaum, W. Zhao, J. Zhang, L. Chen, and C. H. Back, Nat. Commun. **11**, 275 (2020).

[28] S. Bakhtiari, Y. Li, S. Sarkar, H. Yang, L. Cui, and Y. Liu, Mater. Sci. Eng. A-Struct. Mater. Prop. Microstruct. Process. **857**, 144128 (2022).

[29] J. Pfetzing-Micklich, N. Wieczorek, T. Simon, B. Maaß, and G. Eggeler, Mater. Sci. Eng. A-Struct. Mater. Prop. Microstruct. Process. **591**, 33 (2014).

[30] L. Lombardo, G. Toni, F. Stefanoni, F. Mollica, M. P. Guarneri, and G. Siciliani, Angle Orthod. **83**, 298 (2013).

[31] T. Ezaz, J. Wang, H. Sehitoglu, and H. J. Maier, Acta Mater. **61**, 67 (2013).

[32] J. Frenzel, E. P. George, A. Dlouhy, C. Somsen, M. F.-X. Wagner, and G. Eggeler, Acta Mater. **58**, 3444 (2010).

[33] See Supplemental Material at [URL will be inserted by publisher] for a latent-heat thermography movie showing the bending-induced martensitic transition in a NiTi wire.

[34] C. Elibol and M. F.-X. Wagner, Mater. Sci. Eng. A-Struct. Mater. Prop. Microstruct. Process. **621**, 76 (2015).

[35] F. Auricchio and R. L. Taylor, Comput. Meth. Appl. Mech. Eng. **143**, 175 (1997).

[36] L. Torrisi, Bio-Med. Mater. Eng. **9**, 39 (1999).

[37] G. Mani, M. D. Feldman, D. Patel, and C. M. Agrawal, Biomaterials **28**, 1689 (2007).

[38] D. Stoeckel, Minim. Invasive Ther. Allied Technol. **9**, 81 (2000).

[39] H. Fischer, B. Vogel, and A. Welle, Minim. Invasive Ther. Allied Technol. **13**, 248 (2004).

[40] M. Fallot, Ann. Phys. **11**, 291 (1938).

[41] J. S. Kouvel and C. C. Hartelius, J. Appl. Phys. **33**, 1343 (1962).

[42] J. A. Arregi, O. Caha, and V. Uhlíř, Phys. Rev. B **101**, 174413 (2020).

[43] V. Uhlíř, J. A. Arregi, and E. E. Fullerton, Nat. Commun. **7**, 13113 (2016).

[44] G. Li, R. Medapalli, J. Mentink, R. Mikhaylovskiy, T. Blank, S. Patel, A. Zvezdin, T. Rasing, E. Fullerton, and A. Kimel, Nat. Commun. **13**, 2998 (2022).

[45] A. Buzdakov, I. Dolgikh, K. Zvezdin, A. Zvezdin, K. Rubi, U. Zeitler, P. Christianen, T. Rasing, S. Patel, R. Medapalli, *et al.*, Phys. Rev. B **108**, 184420 (2023).

[46] O. Gutfleisch, T. Gottschall, M. Fries, D. Benke, I. Radulov, K. P. Skokov, H. Wende, M. Gruner, M. Acet, P. Entel, *et al.*, Philos. Trans. R. Soc. A-Math. Phys. Eng. Sci. **374**, 20150308 (2016).

[47] H. Straube, J.-M. Wagner, and O. Breitenstein, Appl. Phys. Lett. **95**, 052107 (2009).

[48] S. Daimon, R. Iguchi, T. Hioki, E. Saitoh, and K. Uchida, Nat. Commun. **7**, 13754 (2016).

[49] K. Otsuka and X. Ren, Prog. Mater. Sci. **50**, 511 (2005).

[50] J. M. Jani, M. Leary, A. Subic, and M. A. Gibson, Mater. Des. **56**, 1078 (2014).

[51] L. H. Lewis, C. H. Marrows, and S. Langridge, J. Phys. D-Appl. Phys. **49**, 323002 (2016).

[52] R. Modak, M. Murata, D. Hou, A. Miura, R. Iguchi, B. Xu, R. Guo, J. Shiomi, Y. Sakuraba, and K. Uchida, Appl. Phys. Rev. **9**, 011414 (2022).

[53] C. R. Farrar and K. Worden, Philos. Trans. R. Soc. A-Math. Phys. Eng. Sci. **365**, 303 (2007).

[54] K. T. Butler, D. W. Davies, H. Cartwright, O. Isayev, and A. Walsh, Nature **559**, 547 (2018).

[55] M. Born and E. Wolf, *Principles of optics: electromagnetic theory of propagation, interference and diffraction of light*, 6th ed. (Elsevier, 2013).

[56] L. Rayleigh, Lond. Edinb. Dublin Philos. Mag. J. Sci. **8**, 261 (1879).

[57] J. R. Ferreira-Oliveira, P. C. S. da Silva, L. R. R. de Lucena, R. P. B. dos Reis, C. J. de Araújo, and C. R. B. Filho, Int. J. Thermophys. **42**, 147 (2021).